

Title: Ultrastrongly-coupled magnetochiral magnon-polaritons in metamaterials

Authors: Kentaro Mita¹, Takahiro Chiba^{2,3}, Toshiyuki Kodama⁴, Tetsuya Ueda⁵, Toshihiro Nakanishi⁶, Kei Sawada⁷, Satoshi Tomita^{1,4*}

Affiliations:

¹Department of Physics, Graduate School of Science, Tohoku University; Sendai, Miyagi 980-8576, Japan.

²Frontier Research Institute for Interdisciplinary Sciences, Tohoku University; Sendai, Miyagi 980-8578, Japan.

³Department of Applied Physics, Graduate School of Engineering, Tohoku University; Sendai, Miyagi 980-8579, Japan.

⁴Institute for Excellence in Higher Education, Tohoku University; Sendai, Miyagi 980-8576, Japan.

⁵Department of Electrical Engineering and Electronics, Kyoto Institute of Technology; Sakyo, Kyoto 606-8585, Japan.

⁶Division of Electronic Science and Engineering, Graduate School of Engineering, Kyoto University; Sakyo, Kyoto 615-8515, Japan.

⁷RIKEN SPring-8 Center; Sayo, Hyogo 679-5148, Japan.

*Corresponding author. Email: tomita@tohoku.ac.jp

Abstract: Magnon-polariton is a synthetic quasi-particle of quantized spinwaves in magnets coupled with photons. The recent reporting of ultrastrong photon-to-magnon coupling in magnetic heterostructures was demonstrated at cryogenic temperatures in terms of reciprocal electromagnetic responses. Here, we report that magnon-polaritons in a three-dimensional metamaterial lacking time-reversal and space-inversion symmetries -- magnetochiral magnon-polaritons -- demonstrate ultrastrong coupling and directional non-reciprocity at room temperature. Ultrastrong coupling is due to a direct coupling between microwave photons confined in the chiral meta-atom and magnons in the magnetic meta-atom. Our results reveal a crucial step in identifying cavity-free, deepstrongly-coupled, non-reciprocal magnon-polaritons for hybrid quantum systems and quasi-particle “chemistry” using metamaterials.

One-Sentence Summary: A synthetically engineered metamaterial represents a crucial step toward developing the hybrid quantum systems and quasi-particle “chemistry.”

Main Text:

Introduction

Condensed matter physics is a field of various quasi-particles with elementary excitations. Integrating different quasi-particles has led to novel and intriguing properties of matters and opened an essential pathway toward frontiers (1,2). A magnon, a quantized elementary excitation in magnets, can be transformed to magnon-polariton when it is coupled to alternating current (AC) electromagnetic fields, namely photons. The magnon-polariton has gained attention particularly in quantum information technology and spintronics (3,4) for applications to hybrid quantum systems (5). Magnons and photons are coherently coupled -- strong coupling -- if the coupling constant, g , is larger than the dissipation rate, κ , in a resonator and oscillator ($g > \kappa$), generating magnon-polariton. Here, g is given by $g = (\omega_+ - \omega_-)/2$, where ω_{\pm} is the hybridized eigenmodes at the crossing point of the original mode. Such coherent coupling of magnons with photons with a frequency of $\omega/2\pi$ manifests itself at the anti-crossing of the dispersions together with Rabi-like level repulsion of $2g/2\pi$, which is proportional to a coupling ratio of g/ω . While the strong coupling is characterized by $g > \kappa$, a coherent and ultrastrong magnon-photon coupling represented by $g/\omega > 0.1$ and $g > \kappa$ is indispensable toward the quantum regime (6). Furthermore, the cavity-free magnon-polariton is a central topic in quantum optics as it allows control over individual quantum systems (7,8). The ultrastrongly-coupled magnon-polaritons have been demonstrated at microwave frequencies using magnetic heterostructures composed of superconductors (9-11). They are cavity-free but operated at cryogenic temperatures. Therefore, operating the ultrastrongly-coupled cavity-free magnon-polaritons at room temperature remains challenging.

The ultrastrongly-coupled magnon-polariton is inherently non-reciprocal owing to the breaking of time-reversal symmetry by magnetization or magnetic fields (12). The non-reciprocity results in a transmission amplitude (and phase) difference depending on the propagation direction and polarization of photons. However, such a directionally non-reciprocal optical phenomenon has yet to be observed in ultrastrongly-coupled systems, except for dissipative (13) or strong (14) magnon-photon coupling. Directionally non-reciprocal phenomena exist in natural chiral molecules (15-17), multiferroic materials (18), and metamaterials (19-21) under the external direct current (DC) magnetic fields, as polarization-independent phenomena -- magnetochiral (MCh) and optical magnetoelectric (ME) effects (22,23). Although such non-reciprocal MCh metamaterials indicate the presence of room-temperature coherent couplings between magnons and photons at microwave frequencies (20), the coupling mechanism remains unclear. The coupling mechanism should be therefore clarified by evaluating the coupling ratios of the magnon-polariton.

Here, we demonstrate ultrastrong-couplings of the directionally non-reciprocal magnon-polaritons, referred to as MCh magnon-polaritons, in a single three-dimensional metamolecule at room temperature. The MCh metamolecule consists of a polycrystalline yttrium-iron garnet (YIG) cylinder (as a magnetic meta-atom) inserted in a right-handed helix made of copper (Cu) (as a chiral meta-atom) placed in a microwave waveguide. The metamolecule exhibits MCh magnon-polariton with $g/\omega > 0.2$, indicating the ultrastrong-coupling regime. The ultrastrong coupling is achieved by direct interaction between microwave photons in the Cu chiral structure and magnons in the YIG cylinder. These experimental results are reproduced well via numerical simulations and theoretical consideration.

Experimental results

Figure 1A is an illustration of the MCh metamolecule. The MCh metamolecule is set into a WR-90 waveguide that supports the TE₁₀ mode (Fig. 1B). The metamolecule is parallel to the x -axis; the molecular orientation differs from that of a previous study (20). An external DC magnetic field, $\mu_0 H_{\text{ext}}$, up to approximately 540 mT, is applied in the $+z$ -direction by an electromagnet. All measurements are carried out at room temperature. Figure S1 presents more details of the sample preparation, measurement setup, and microwave propagation mode. Figure 1C illustrates the transmission amplitude $|S_{21}|$ spectra of the MCh metamolecule from 7 to 14 GHz under varying $\mu_0 H_{\text{ext}}$ (0-543 mT) measured using a vector network analyzer. Without the DC magnetic field ($\mu_0 H_{\text{ext}} = 0$), two sharp dips are observed: one at 9.34 GHz (a) and the other at 12.36 GHz (b). Based on numerical simulation using COMSOL Multiphysics of the metamolecule under $\mu_0 H_{\text{ext}} = 0$, we confirm that a dip at the lowest frequency is traced back to the third-order resonance, with two nodes in the Cu chiral meta-atom induced by the microwave photons with the AC magnetic field in the x -axis (Fig. S2A and Movie S1). Thus, the dip (a) at 9.34 GHz is traced back to the resonating photons, referred to as chiral cavity photons. Contrastingly, a dip at the higher frequency is not caused by simple resonance but by a complex mode with tornado-like current distribution in the Cu chiral structure or Mie resonance by the displaced YIG cylinder (Figs. S2A and S2C and Movie S2). Therefore, in this experiment, we focus on the third-order chiral cavity photon at approximately 9 GHz, which is labeled as (a).

Applying the external DC magnetic field to the metamolecule in the $+z$ -direction causes the chiral cavity photon mode (a) to shift slightly to a lower frequency at $\mu_0 H_{\text{ext}} = 61$ mT and then turn to a higher frequency at $\mu_0 H_{\text{ext}} = 251$ mT. The major blue shift of the chiral cavity photon mode is attributed to the magnetic permeability change of the YIG cylinder by the applied $\mu_0 H_{\text{ext}}$ (20,21), which is the evidence of the interaction between the YIG magnetic meta-atom and the microwave photon in the Cu chiral meta-atom. When $\mu_0 H_{\text{ext}} = 312$ mT, a slight dip appears at approximately 8 GHz labeled as (c) in Fig. 1C. The slight dip keeps moving to a higher frequency with an increase in $\mu_0 H_{\text{ext}}$ up to 543 mT; therefore, the dip is caused by ferromagnetic resonance, i.e., a magnon, in the YIG magnetic meta-atom. When $\mu_0 H_{\text{ext}} = 339$ mT, the magnon mode (c) approaches the chiral cavity photon mode (a). Simultaneously, another sharp dip appears at 7.19 GHz, denoted by (a'), and shifts to a higher frequency with a further increase in $\mu_0 H_{\text{ext}}$. This indicates the hybridization of chiral cavity photon modes (a) and (a') with the magnon mode (c), demonstrating the coherent coupling between chiral cavity photons and magnons in the metamolecule.

$|S_{21}|$ is plotted two-dimensionally in Fig. 2A as functions of $\mu_0 H_{\text{ext}}$ of 0-543 mT (horizontal axis) and of frequency of 7-14 GHz (vertical axis) to evaluate magnon-photon coupling strength. The black color corresponds to a higher transmission in the $|S_{21}|$ spectra, while the yellow to white colors correspond to lower transmissions. Green dotted lines correspond to eye guides of the chiral cavity photon frequency and the magnon dispersion. The $|S_{21}|$ two-dimensional (2D) plot in Fig. 2A highlights, at $\mu_0 H_{\text{ext}} \sim 350$ mT, the anti-crossing between the chiral cavity photon mode (a) with $\omega_a/2\pi = 9.34$ GHz and magnon mode (c). The anti-crossing Rabi-like level splitting of chiral cavity photon modes (a) and (a') is $g/\pi = 4.19$ GHz at $\mu_0 H_{\text{ext}} = 367.7$ mT, resulting in a coupling ratio of $g/\omega_a = 0.22$. Figure 2A demonstrates that magnons in the YIG cylinder and photons in the Cu chiral structure in the MCh metamolecule are ultra-strongly coupled at room temperature. The metamolecule orientation can change the coupling ratio. Figures S3A, S3B, and S3C indicate that the z -axis-orientated metamolecule has a smaller coupling. Thus, the coupling ratio is relevant to the electromagnetic mode.

Figures S4A and S4B present the directional transmission amplitude difference, $|S_{21}| - |S_{12}|$, and phase difference, $\arg S_{21} - \arg S_{12}$, spectra of the MCh metamolecule in the x -axis orientation, respectively. A 2D plot of experimentally observed $|S_{21}| - |S_{12}|$ is drawn in Fig. 2B using Fig. S4A. The red color corresponds to $|S_{21}| > |S_{12}|$, while the blue color corresponds to $|S_{21}| < |S_{12}|$. The chiral cavity photon mode (a) above the magnon mode line (c) demonstrates $|S_{21}| < |S_{12}|$, while the mode (a') below the magnon mode (c) represents $|S_{21}| > |S_{12}|$. This is characteristic of the directional non-reciprocity of ultrastrongly-coupled magnon-polariton.

Numerical simulations

Simultaneous breaking of time-reversal and space-inversion symmetries by the coexistence of magnetism and chirality in the metamolecule is the primary origin of the directional non-reciprocity (Fig. 2B). An alternative and artificial origin could be a slight displacement of the metamolecule from the waveguide center or a misalignment of the metamolecule from the x -axis because similar non-reciprocal signals have been observed by an asymmetrical microstrip line on a ferrite substrate (24) and a displaced magnetic material on a coplanar waveguide (25). In this study, numerical simulation indicates that the dip (b) observed at a higher frequency is caused by the Mie resonance of the displaced YIG cylinder (Figs. S2A and S2C). We conduct numerical simulations of the metamolecule under various magnetic fields using COMSOL Multiphysics to exclude such an artificial origin. The Supplementary Material details the numerical simulation method.

Figure 2C presents a numerically simulated 2D plot of $|S_{21}|$ as functions of $\mu_0 H_{\text{ext}}$ of 200-600 mT (horizontal axis) and of 7-14 GHz frequency (vertical axis). Level repulsion due to the interaction between chiral cavity photons (d and d') and magnons (e) is reproduced (Fig. 2C). The simulated coupling ratio of 0.15 derived from the level splitting of 3.21 GHz at $\mu_0 H_{\text{ext}} = 410$ mT is smaller than that observed experimentally in Fig. 2A because the magnetization dynamics in the YIG cylinder is linearized in the numerical simulation. Nevertheless, the simulated 2D plot of $|S_{21}| - |S_{12}|$ in Fig. 2D has successfully reproduced the directional non-reciprocity of the magnon-polariton between modes (d) and (d'). The metamolecule has negligible dissipation and is regarded as a Hermitian system. Removal of the misalignment and displacement of the metamolecule in the simulation (Fig. 2D) verifies that the origin of directionally non-reciprocal signals is the MCh magnon-polariton under the simultaneous breaking of time-reversal and space-inversion symmetries in the metamolecule.

Theoretical considerations

The coupling ratio of MCh magnon-polariton is quantitatively reproduced by considering the magnetization dynamics. The experimental system is the forced oscillation of magnon-polaritons driven by the input microwaves; nonetheless, a simpler damped oscillation model is assumed to evaluate the coupling ratio of the magnon and chiral cavity photons. As in Fig. 3A, $h_{n,x}$ represents an AC magnetic field in the x -direction due to the Faraday electromagnetic induction in the chiral meta-atom -- chiral cavity photons. Here, the integer n denotes the mode-index of the chiral cavity photons. The AC magnetic field $h_{n,x}$ excites magnons (m_x) in the YIG cylinder. This leads to direct coupling between magnons and chiral cavity photons, generating magnon-polaritons in the metamolecule. Recall that the numerical simulation using COMSOL indicates that the third-order resonance with $n = 3$ ($h_{3,x}$) appears at approximately 10 GHz. Thus, the magnon-polaritons can be described as a coupled oscillator model that considers a uniform magnon mode and two chiral photon modes with $n = 3$ and 5. The Supplementary Material presents the calculation details.

Figures 3B and 3C are calculated damped oscillations of the chiral cavity photons ($h_{n,x}$) and the magnons (m_x) under $\mu_0 H_{\text{ext}} = 0.39$ T for $n = 3$ and under $\mu_0 H_{\text{ext}} = 0.50$ T for $n = 5$, respectively. We assume the higher frequency mode to be the fifth-order resonance. The time evolutions in Figs. 3B and 3C correspond to Rabi-like oscillations -- the amplitude exchange between one chiral cavity photon and a magnon. A minimal complexity in the Rabi-like oscillations is attributed to interactions among three modes (one magnon and two chiral cavity photons) in the metamolecule. Figures 3D and 3E correspond to the Fourier spectra of the time evolutions, in which three peaks represent coupled modes among one magnon and two chiral cavity photons, i.e., magnon-polariton modes with the Rabi-like frequency splitting. According to these spectra, the evaluated couplings are $g_3/\pi = 3.75$ GHz and $g_5/\pi = 3.93$ GHz, resulting in the coupling ratios of $g_3/\omega_3 = 0.20$ and $g_5/\omega_5 = 0.16$, respectively. Here, the subscripts in g_n and ω_n mean the corresponding values of the n -th order. Based on the experimental results, $\omega_3/2\pi = 9.34$ and $\omega_5/2\pi = 12.36$ GHz are assumed for this evaluation. The computed $g_3/\omega_3 = 0.20$ is consistent with the experimentally obtained $g/\omega_a = 0.22$, indicating that magnon-polariton in the MCh metamolecule is in the ultrastrong coupling regime. Moreover, $g_3/\omega_3 = 0.20$ and $g_5/\omega_5 = 0.16$ indicate that the coupling at a lower frequency is much stronger than that at a higher frequency.

Discussion and perspective

This study reveals that the MCh metamolecule consisting of a YIG cylinder inserted in a Cu chiral structure results in ultra-strongly coupled and non-reciprocal MCh magnon-polariton at room temperature. Table S1 compares the temperature, cavity-free, magnon-polariton coupling ratio, and non-reciprocity obtained in this study with those reported in the literature. Ultrastrong coupling in the magnon-polariton is primarily caused by direct interaction between photons in the Cu chiral structure and magnons in the magnetic YIG cylinder via AC magnetic fields in the x -direction. The coupling ratio is reduced in the z -axis-orientated metamolecule (Fig. S3C) because electromagnetically induced AC magnetic fields in the z -direction cannot drive magnons under the external DC magnetic field, $\mu_0 H_{\text{ext}}$, in the z -direction. This results in indirect coupling between the chiral cavity photon and magnon in the z -axis-orientated metamolecule. Therefore, the coupling ratio can be enhanced by finding a suitable metamolecule orientation.

The second origin of the ultrastrong coupling is the photon confinement in the chiral meta-atom. The chiral meta-atom functions as a resonator or sensitizer; therefore, the MCh metamolecule realizes cavity-free magnon-polariton for the propagating microwave in the free space. In addition to controlling individual quantum systems (7,8), the MCh magnon-polariton in the free space leads to the observation of the polarization-independent optically-moving magnon-polariton. The optically-moving effect in the MCh and ME media exhibits an electromagnetic response equivalent to that of a regular material moving at a relativistic speed (26,27). A free-space measurement would enable us to observe the optically-moving magnon-polariton. The Hermitian, ultrastrongly-coupled, and optically-moving magnon-polariton may give rise to coherent quantum rectification of quantum information.

Utilizing the fundamental mode ($n = 1$) is a strategy toward achieving a much stronger coupling between magnons and photons – the deepstrongly-coupled magnon-polariton, i.e., $g/\omega_a \geq 1$, in the metamolecule. This experiment uses the third-order mode ($n = 3$) of the chiral cavity photon to obtain the highest value of $g/\omega_a = 0.22$; thus, the magnon-photon coupling is reduced by $\eta_3 = 1/3$, where η_n is a phenomenologically introduced mode-dependent coefficient responsible for the space-dependence of the microwave magnetic field in the MCh metamolecule. Here, we assume the net magnitude of the AC magnetic field of the chiral photon to be inversely proportional to

the number of antinodes (theoretical consideration in the Supplementary Material). This way, the $n = 1$ fundamental mode may enhance the magnon-photon coupling by maximizing the electromagnetic induction due to the magnon dynamics. Additionally, according to the theoretical prediction for the metamolecule (28), the coupling ratio is evaluated via $g/\omega_a \propto 1/\sqrt{\omega_a}$. Thus, further enhancement toward the deepstrong-coupling is possible by decreasing the chiral resonant frequency, ω_a , of the fundamental mode by reducing the system size and changing the design of the metamolecule and materials of the constitutive meta-atoms. The deepstrongly-coupled magnon-polariton will lead to mysterious quantum effects, such as the vacuum Bloch-Siegert shift (29), the super-radiant phase transition (30), and quantum squeezing under thermal equilibrium (31).

This study demonstrates that metamaterials are promising for integrating different quasi-particles. One quasi-particle is embodied by one meta-atom; therefore, the synthesis of metamolecules and metamaterials by combining different meta-atoms leads to quasi-particle integration. The quasi-particle integration is comprehensively classified according to the interaction between polarization P and magnetization M . The conventional ME and MCh effects are given by the coupling between P and M . Contrastingly, the dynamic coupling of time-derivatives of P and M results in a new collective mode corresponding to an MCh electromagnon-polariton, which is anticipated to be observed using metamaterials. Furthermore, we focus on magnons in this study; however, other quasi-particles, such as, excitons, phonons, and plasmons, can be integrated into the metamaterials. Thus, this study signifies a pivotal advancement toward expounding quasi-particle “chemistry” using metamaterials.

References and Notes

1. A. F. Kockum, A. Miranowicz, S. De Liberato, S. Savasta, F. Nori, Ultrastrong coupling between light and matter. *Nature Reviews Physics* **1**, 19 (2019).
2. P. Forn-Díaz, L. Lamata, E. Rico, J. Kono, E. Solano, Ultrastrong coupling regimes of light-matter interaction. *Reviews of Modern Physics* **91**, 025005 (2019).
3. Y. Li, W. Zhang, V. Tyberkevych, W.-K. Kwok, A. Hoffmann, V. Novosad, Hybrid magnonics: physics, circuits, and applications for coherent information processing. *Journal of Applied Physics* **128**, 130902 (2020).
4. M. Harder, B. M. Yao, Y. S. Gui, C.-M. H, Coherent and dissipative cavity magnonics. *Journal of Applied Physics* **129**, 201101 (2021).
5. D. Lachance-Quirion, Y. Tabuchi, A. Gloppe, K. Usami, Y. Nakamura, Hybrid quantum systems based on magnonics. *Applied Physics Express* **12**, 070101 (2019).
6. G. Bourcin, J. Bourhill, V. Vlaminck, V. Castel, Strong to ultrastrong coherent coupling measurements in a YIG/cavity system at room temperature *Physical Review B* **107**, 214423 (2023).
7. A. Bayer, M. Pozimski, S. Schambeck, D. Schuh, R. Huber, D. Bougeard, C. Lange, Terahertz Light–Matter Interaction beyond Unity Coupling Strength. *Nano Letters* **17**, 6340–6344 (2017).

8. S. Rajabali, S. Markmann, E. Jöchl, M. Beck, C. A. Lehner, W. Wegscheider, J. Faist, G. Scalari, An ultrastrongly coupled single terahertz meta-atom. *Nature communications* **13**, 2528 (2022).
9. I. Golovchanskiy, N. N. Abramov, V. S. Stolyarov, A. A. Golubov, M. Yu. Kupriyanov, V.V. Ryazanov, A. V. Ustinov, Approaching Deep-Strong On-Chip Photon-To-Magnon Coupling, *Physical Review Applied* **16**, 034029 (2021).
10. I. A. Golovchanskiy, N. N. Abramov, V. S. Stolyarov, M. Weides, V. V. Ryazanov, A. A. Golubov, A. V. Ustinov, M. Y. Kupriyanov, Ultrastrong photon-to-magnon coupling in multilayered heterostructures involving superconducting coherence via ferromagnetic layers. *Science Advances* **7**, eabe8638 (2021).
11. A. Ghirri, C. Bonizzoni, M. Maksutoglu, A. Mercurio, O. Di Stefano, S. Savasta, M. Affronte, Ultrastrong Magnon-Photon Coupling Achieved by Magnetic Films in Contact with Superconducting Resonators. *Physical Review Applied* **20**, 024039 (2023).
12. M. Harder, C.-M. Hu, Chapter Two - Cavity Spintronics: An Early Review of Recent Progress in the Study of Magnon-Photon Level Repulsion. *Solid State Physics* **69**, 47 (2018).
13. M. M. Harder, Y. Yang, B. M. Yao, C. H. Yu, J. W. Rao, Y. S. Gui, R. L. Stamps, C. M. Hu, Level Attraction Due to Dissipative Magnon-Photon Coupling. *Physical Review Letters* **121**, 137203 (2018).
14. X. Zhang, A. Galda, X. Han, D. Jin, V. M. Vinokur, Broadband Nonreciprocity Enabled by Strong Coupling of Magnons and Microwave Photons. *Physical Review Applied* **13**, 044039 (2020).
15. L. D. Barron, J. Vrbancich, Magneto-chiral birefringence and dichroism. *Molecular Physics* **51**, 715 (1984).
16. G. L. J. A. Rikken, E. Raupach, Observation of magneto-chiral dichroism. *Nature* **390**, 493 (1997).
17. M. Vallet, R. Ghosh, A. Le Floch, T. Ruchon, F. Bretenaker, J.-Y. Thépot, Observation of Magnetochiral Birefringence. *Physical Review Letters* **87**, 183003 (2001).
18. Y. Okamura, F. Kagawa, S. Seki, M. Kubota, M. Kawasaki, Y. Tokura, Microwave Magnetochiral Dichroism in the Chiral-Lattice Magnet Cu_2OSeO_3 . *Physical Review Letters* **114**, 197202 (2015).
19. S. Tomita, K. Sawada, A. Porokhnyuk, T. Ueda, Direct observation of magnetochiral effects through a single metamolecule in microwave regions. *Physical Review Letters* **113**, 235501 (2014).
20. S. Tomita, H. Kurosawa, K. Sawada, T. Ueda, Enhanced magnetochiral effects at microwave frequencies by a single metamolecule. *Physical Reviews B* **95**, 085402 (2017).
21. S. Tomita, H. Kurosawa, T. Ueda, K. Sawada, Metamaterials with magnetism and chirality. *Journal of Physics D: Applied Physics* **51**, 083001 (2018).
22. Y. Tokura, N. Nagaosa, Nonreciprocal responses from non-centrosymmetric quantum materials. *Nature Communication* **9**, 3740 (2018).
23. S. Toyoda, N. Abe, T. Arima, Nonreciprocal Refraction of Light in a Magnetoelectric Material. *Physical Review Letters* **123**, 077401 (2019).

24. T. Ueda, M. Tsutsumi, Left-Handed Transmission Characteristics of Ferrite Microstrip Lines without Series Capacitive Loading. *IEICE Transactions on Electronics* **E89-C**, 1318–23 (2006).
25. T. Kodama, Y. Kusanagi, S. Okamoto, N. Kikuchi, O. Kitakami, S. Tomita, N. Hosoito, H. Yanagi, Microwave Spectroscopy of a Single Permalloy Chiral Metamolecule on a Coplanar Waveguide, *Physical Review Applied* **9**, 054025 (2018).
26. J. A. Kong, *Electromagnetic Wave Theory* (EMW Publishing, Cambridge, 2005).
27. V. S. Asadchy, A. Díaz-Rubio, S. A. Tretyakov, Bianisotropic metasurfaces: physics and applications. *Nanophotonics* **7**, 1069 (2018).
28. T. Chiba, T. Komine, T. Aono, Microwave Transmission Theory for On-Chip Ultrastrong-Coupled Magnon-Polariton in Dynamical Inductors. *Journal of the Magnetism Society of Japan* **48**, 21 (2024).
29. X. Li, M. Bamba, Q. Zhang, S. Fallahi, G. C. Gardner, W. Gao, M. Lou, K. Yoshioka, M. J. Manfra, J. Kono, Vacuum Bloch–Siegert shift in Landau polaritons with ultra-high cooperativity. *Nature Photonics* **12**, 324 (2018).
30. D. Kim, S. Dasgupta, X. Ma, J. -M. Park, H. -T. Wei, L. Luo, J. Doumani, X. Li, W. Yang, D. Cheng, R. H. J. Kim, H. O. Everitt, S. Kimura, H. Nojiri, J. Wang, S. Cao, M. Bamba, K. R. A. Hazzard, J. Kono, Observation of the Magnonic Dicke Superradiant Phase Transition. *arXiv*: 2401.01873.
31. K. Hayashida, T. Makihara, N. Marquez Peraca, D. Fallas Padilla, H. Pu, J. Kono, M. Bamba, Perfect intrinsic squeezing at the superradiant phase transition critical point. *Scientific Reports* **13**, 2526 (2023).
32. D. M. Pozar, *Microwave Engineering 3rd. Edition* (John Wiley & Sons, 2025).
33. Y. Cao, L. He, P. Zhuang, Solid-state calculation of crystalline color superconductivity. *Physical Review D* **91**, 094423 (2015).
34. X. Zhang, M. Sarovar, Quantum Hamiltonian Identification from Measurement Time Traces. *Physical Review Letters* **113**, 156401 (2014).
35. L. Bai, M. Harder, Y. P. Chen, X. Fan, J. Q. Xiao, C.-M. Hu, Spin Pumping in Electrostatically Coupled Magnon-Photon Systems. *Physical Review Letters* **114**, 227201 (2015).

Acknowledgments: We thank H. Yasuda and Y. Motoda for their technical support with the microwave measurements and H. Kurosawa for helping with the numerical simulation. We would like to thank Editage for English language editing.

Funding:

Japan Society for the Promotion of Science (JSPS) KAKENHI No. JP24H02232 (ST)
 JSPS KAKENHI No. 23K13621 (TK)
 JSPS KAKENHI No. 22K14591 (TC)
 Japan Science and Technology Agency (JST) CREST No. JPMJCR2102 (ST)

Author contributions:

Conceptualization: TC, ST

Methodology: KM, TC, TK, TU, ST

Investigation and Visualization: KM, TC, TK

Funding acquisition: TC, TK, ST

Project administration: ST

Supervision: TU, TN, KS, ST

Writing – original draft: KM, TC, ST

Writing – review & editing: All authors

Competing interests: The authors declare that they have no competing interests.

Data and materials availability: All data are available in the main text or the supplementary material.

Supplementary Material

Materials and Methods

Supplementary Text

Figs. S1 to S4

Table S1

References (32–35)

Movies S1 and S2

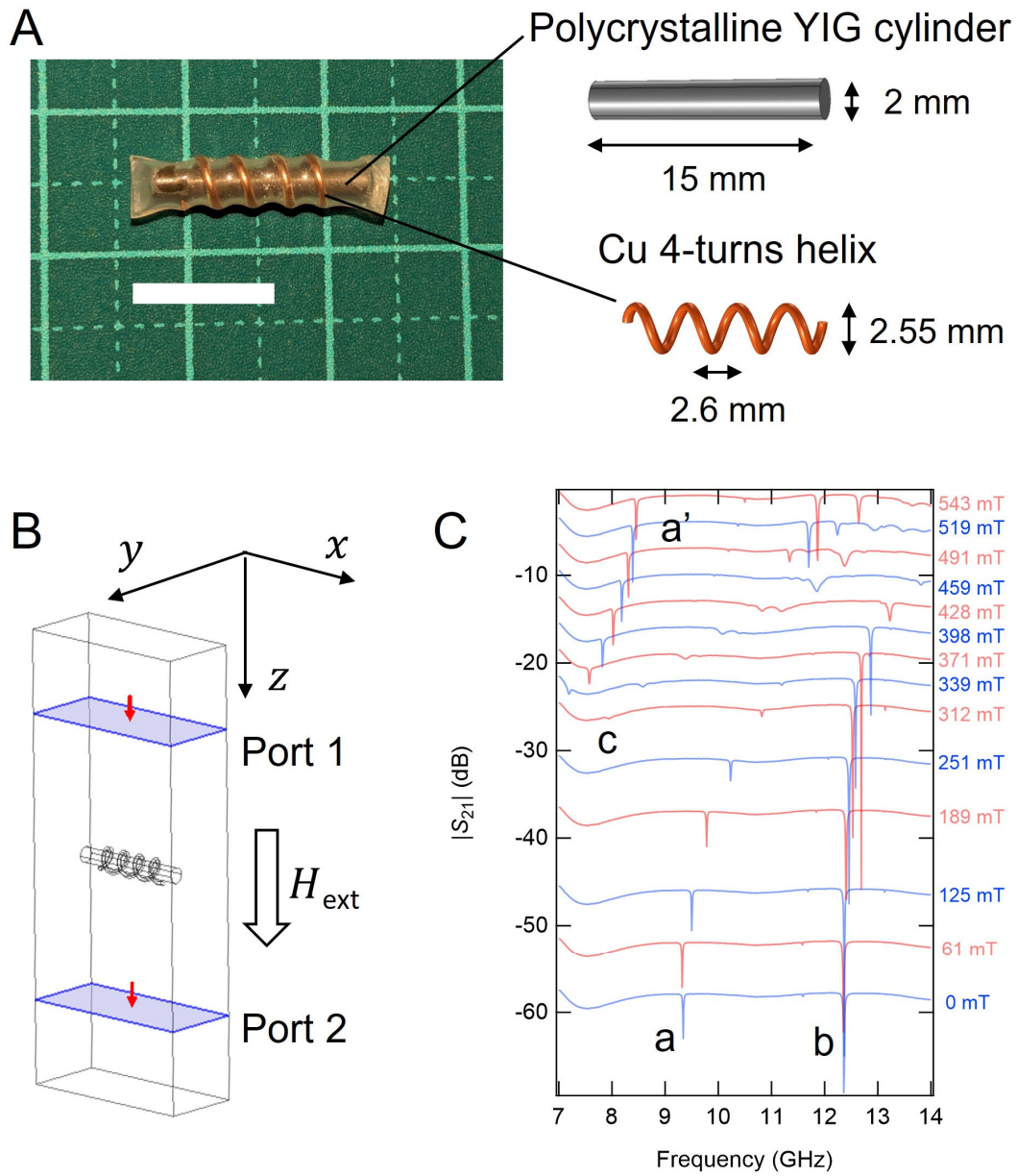


Fig. 1. Magneto-chiral (MCh) metamolecule under study, measurement setup, and measured microwave spectra of the metamolecule. (A) Sample photo and constituents. A white bar corresponding to 10 mm. (B) Measurement setup of x -axis oriented metamolecule placed in a waveguide. (C) $|S_{21}|$ amplitude spectra of x -axis oriented metamolecule under various magnetic fields.

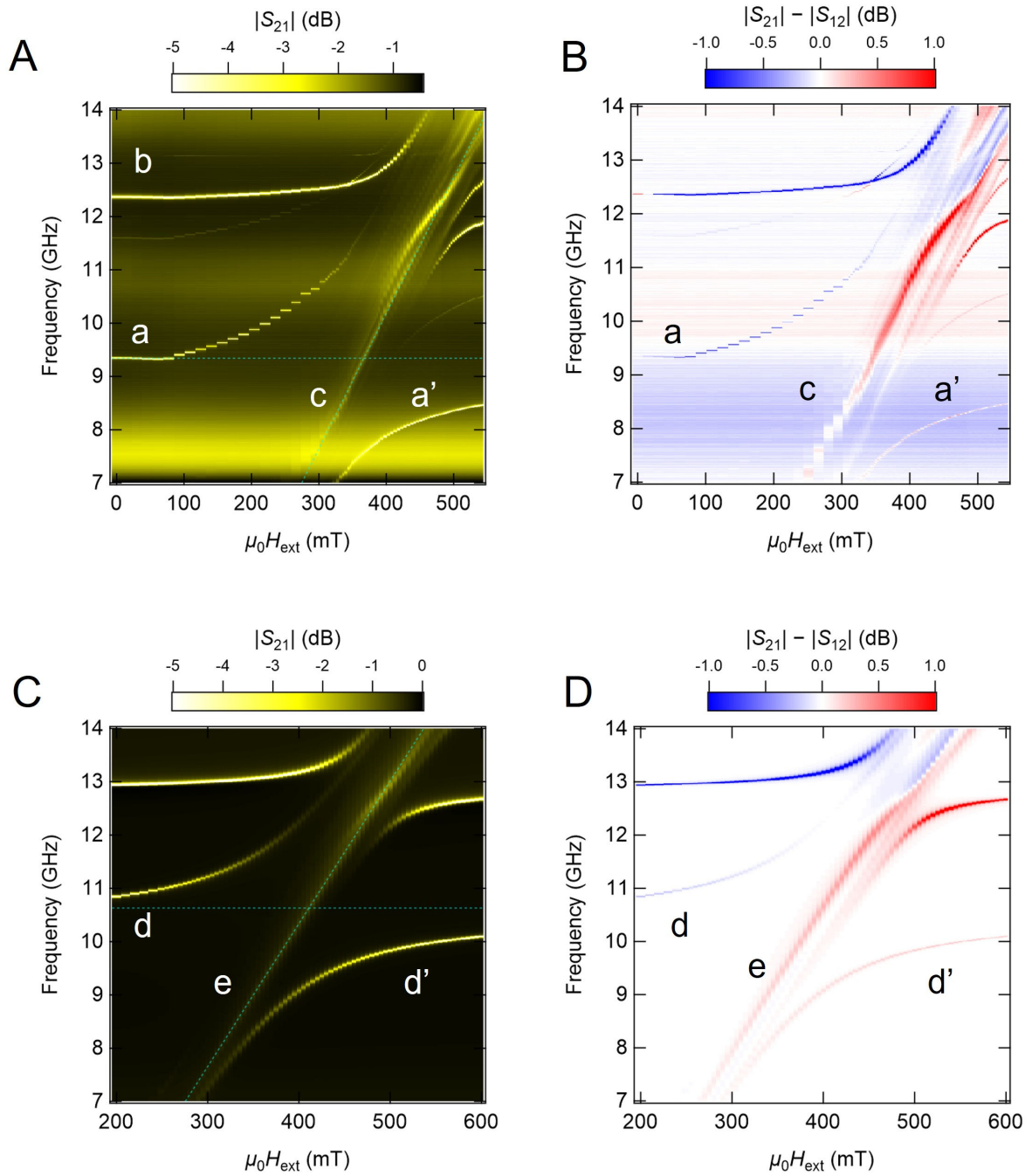


Fig. 2. Two dimensional plot of measured and simulated magnon-polariton dispersions. Measured 2D plots of (A) transmission amplitude $|S_{21}|$ and (B) amplitude difference $|S_{21}| - |S_{12}|$ of x -axis oriented metamolecule as functions of applied external DC magnetic field, $\mu_0 H_{\text{ext}}$, and frequency. (C) and (D) are 2D plots numerically simulated using COMSOL Multiphysics, corresponding to (A) and (B), respectively.

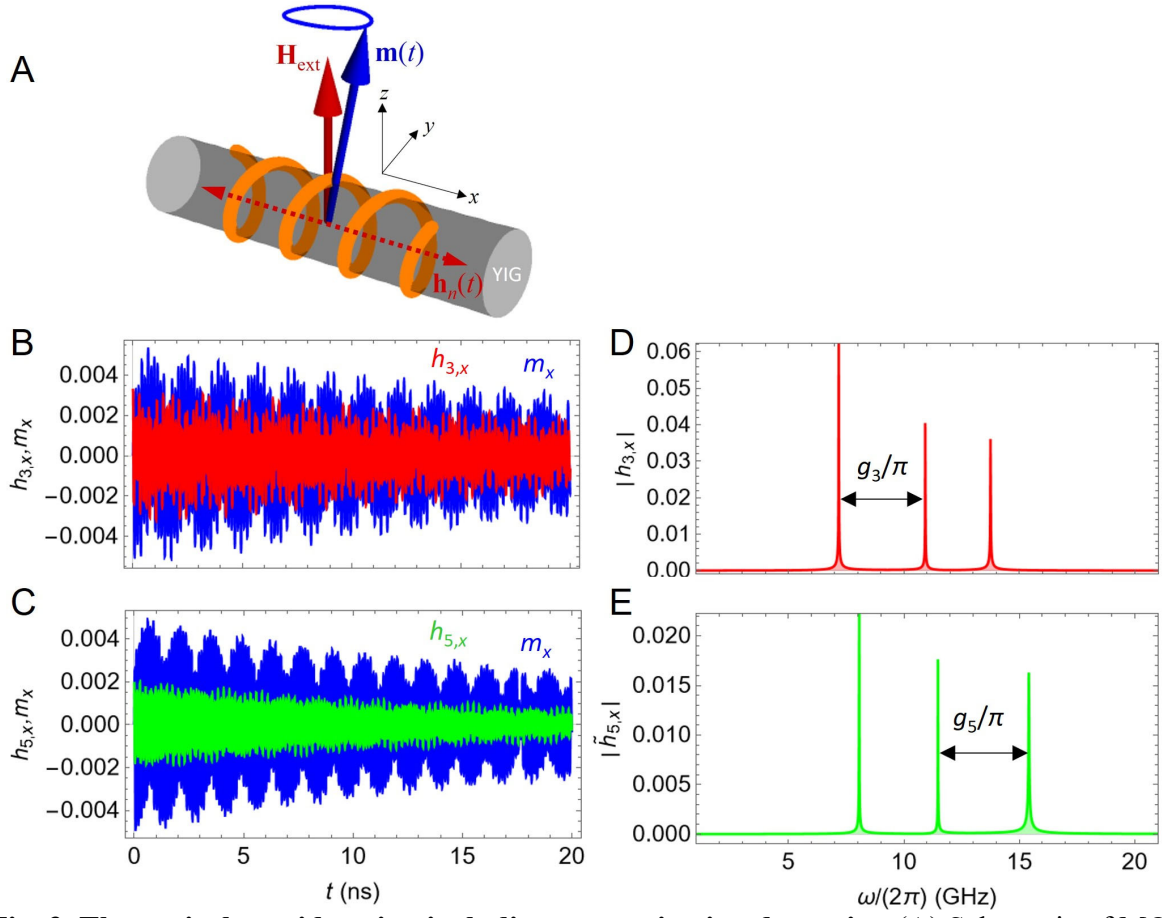


Fig. 3. Theoretical consideration including magnetization dynamics. (A) Schematic of MCh metamolecule composed of a Cu chiral structure involving a YIG cylinder. The metamolecule's YIG cylinder is oriented to the x -axis. (B) and (C) Rabi-like oscillations of the chiral cavity photons ($h_{n,x}$) and magnon (m_x) under $\mu_0 H_{\text{ext}} = 0.39$ T ($n = 3$) and $\mu_0 H_{\text{ext}} = 0.50$ T ($n = 5$), respectively. (D) and (E) Corresponding Fourier spectra of chiral cavity photons ($h_{n,x}$) for 9.34 GHz and 12.36 GHz, respectively.

Supplementary Materials for

Ultrastrongly-coupled magnetochiral magnon-polaritons in metamaterials

Kentaro Mita, Takahiro Chiba, Toshiyuki Kodama, Tetsuya Ueda, Toshihiro Nakanishi, Kei Sawada, Satoshi Tomita

Corresponding author: Satoshi Tomita tomita@tohoku.ac.jp

The PDF file includes:

Materials and Methods
Supplementary Text
Figs. S1 to S4
Table S1
References (32-35)

Other Supplementary Materials for this manuscript include the following:

Materials and Methods

Metamolecule preparation and measurement setup

The MCh metamolecule consists of a polycrystalline YIG cylinder as the magnetic meta-atom inserted in a right-handed helix made of Cu as the chiral meta-atom. The YIG cylinder is 2 and 15 mm in diameter and length, respectively. The Cu wire of 0.55 mm diameter is wounded four times with a 2.6 mm pitch to form the right-handed helix of a 2.55 mm outer diameter. The MCh metamolecule is set into a WR-90 waveguide that supports the TE₁₀ mode with square flange adapters (Pasternack PE9804). The metamolecule is oriented along the x - or z -axis. A DC magnetic field, $\mu_0 H_{\text{ext}}$, up to approximately 540 mT is applied in the $+z$ direction by an electromagnet. The waveguide is connected to a vector network analyzer (VNA) (Rohde&Schwarz ZVA67) with a microwave input power of 0 dBm (1mW). The S parameters are measured using VNA. The S_{21} indicates a complex transmission coefficient from port 1 to 2, while S_{12} represents that from port 2 to 1 (Figs. 1B and S3A). All measurements are carried out at room temperature.

AC magnetic and electric fields of the TE₁₀ mode in the WR-90 waveguide

Figure S1 presents an overview of the AC magnetic and electric fields of the TE₁₀ mode in the WR-90 waveguide. An MCh metamolecule oriented to the x -axis is placed at the center of the waveguide. The microwave travels in the z -direction. Figure S1A presents a snapshot of numerically simulated AC magnetic and electric fields (blue and red arrows, respectively). Figure S1B shows an x - z plane view of the AC magnetic fields in the z -direction at the metamolecule. Figures S1C and S1D present the x - y plane views of the AC magnetic and electric fields, respectively. Figure S1C reveals that the AC magnetic field is along the x -direction, while Fig. S1D reveals that the AC electric field is along the y -direction. For the x -axis oriented metamolecule at the waveguide center, the microwave's AC magnetic fields in the x -direction induce electromagnetic induction in the chiral structure, resulting in AC magnetic fields in the x -direction (chiral cavity photons) that excite a magnon in the YIG cylinder under external DC magnetic field, H_{ext} , in the z -direction.

Numerical simulation using COMSOL Multiphysics

The maximum size of the mesh in the simulation space is limited to $\lambda/10$ mm, where λ mm is the wavelength of the electromagnetic wave. The direct solver mode is used, and Fig. 1B illustrates the simulation model. The cross-section of the simulation space is 10.16 mm x 22.86 mm, corresponding to that of the WR-90 waveguide. The x - z and y - z planes are represented by perfect electric conductors. The metamolecule is placed at the center of the waveguide and sandwiched by air layers followed by perfectly matched layers. The thicknesses of the air and perfectly matched layers in the z -direction are $\lambda/15$ mm and $\lambda/2$ mm, respectively.

The surface of the chiral structure is represented by a perfect electric conductor. Contrastingly, the YIG cylinder has zero electric conductivity with isotropic permittivity of $14.5 - j 0.0036$ (32), where $j = \sqrt{-1}$ corresponds to an imaginary number unit. The permeability of the YIG cylinder on the ferromagnetic resonance (FMR) is described as follows. The angular frequency of FMR (ω_{FMR}) of the magnetic cylinder under external DC magnetic fields, $\mu_0 H_{\text{ext}}$, is represented by the Kittel equation:

$$\omega_{\text{FMR}} = \gamma \sqrt{\mu_0 H_{\text{ext}} (\mu_0 H_{\text{ext}} - \mu_0 M_{\text{eff}})}, \quad (\text{S1})$$

where μ_0 corresponds to the permeability of the vacuum. Saturation magnetization, $\mu_0 M_S$, is set to 200 mT based on previous magnetization measurements (19). The effective magnetization,

$\mu_0 M_{\text{eff}}$, is set to $0.521 \times \mu_0 M_S = 104$ mT to reproduce the FMR frequency observed in this experiment. When magnetization is in the z -direction, the relative permeability tensor $\tilde{\mu}_r$ is expressed as

$$\tilde{\mu}_r = \begin{pmatrix} \mu_r^{\text{xx}} & \mu_r^{\text{xy}} & 0 \\ \mu_r^{\text{yx}} & \mu_r^{\text{yy}} & 0 \\ 0 & 0 & 1 \end{pmatrix}, \quad (\text{S2})$$

where

$$\begin{aligned} \mu_r^{\text{xx}} &= \mu_r^{\text{yy}} \\ &= 1 + \gamma \mu_0 M_{\text{eff}} \frac{[\omega_{\text{FMR}}(\omega_{\text{FMR}}^2 - \omega^2) + \omega_{\text{FMR}} \omega^2 \alpha^2]}{\left[(\omega_{\text{FMR}}^2 - \omega^2(1 + \alpha^2))^2 + 4\omega_{\text{FMR}}^2 \omega^2 \alpha^2 \right]} \\ &\quad - j\gamma \mu_0 M_{\text{eff}} \frac{\alpha \omega [\omega_{\text{FMR}}^2 + \omega^2(1 + \alpha^2)]}{\left[(\omega_{\text{FMR}}^2 - \omega^2(1 + \alpha^2))^2 + 4\omega_{\text{FMR}}^2 \omega^2 \alpha^2 \right]}, \end{aligned} \quad (\text{S3})$$

and

$$\begin{aligned} \mu_r^{\text{xy}} &= -\mu_r^{\text{yx}} \\ &= 2\gamma \mu_0 M_{\text{eff}} \frac{\omega_{\text{FMR}} \omega^2 \alpha}{\left[(\omega_{\text{FMR}}^2 - \omega^2(1 + \alpha^2))^2 + 4\omega_{\text{FMR}}^2 \omega^2 \alpha^2 \right]} \\ &\quad + j\gamma \mu_0 M_{\text{eff}} \frac{\omega [\omega_{\text{FMR}}^2 - \omega^2(1 + \alpha^2)]}{\left[(\omega_{\text{FMR}}^2 - \omega^2(1 + \alpha^2))^2 + 4\omega_{\text{FMR}}^2 \omega^2 \alpha^2 \right]}. \end{aligned} \quad (\text{S4})$$

γ corresponds to the gyromagnetic ratio, and α is to the phenomenological Gilbert damping parameter. α is 0.01 in this simulation. The S parameter spectra were 7-14 GHz under various $\mu_0 H_{\text{ext}}$, from 200 to 600 mT, in 5 mT intervals, and we prepared 2D plots (Figs. 2C and 2D).

Theoretical consideration based on a coupled oscillator model

We describe magnon-polaritons in the MCh metamolecule based on a coupled oscillator model that considers a uniform magnon mode and two chiral photon modes. Figure S1 illustrates the system, in which the magnetization of a YIG cylinder is excited by the AC resonant magnetic fields, $\mathbf{H}_n(t)$, with the resonant modes ω_n (n denotes the mode index). Instead of the experimental system, which is the forced oscillation of magnon-polaritons driven by the input microwaves from VNA, we introduce a simpler damped oscillation model to evaluate the coupling ratio between the magnon and chiral cavity photons. In the absence of the photon's damping, the AC resonant magnetic field could consist only of the x -component, which is decomposed into $\mathbf{H}_n(t) = \eta_n \mathbf{H}_0(t) = \eta_n H_0(t) \hat{\mathbf{x}}$. $H_0(t) = H_0 \exp(-i\omega_n t)$ and η_n is a phenomenologically introduced mode-dependent coefficient responsible for the space-dependence of the microwave magnetic field in the MCh metamolecule. The resonant AC magnetic fields of the chiral cavity photons are coupled to magnetization dynamics $\mathbf{M}_n(t)$ with the magnon's modes via the Zeeman interaction. According to the above ansatz regarding the η_n coefficient, the magnetization dynamics can be written as $\mathbf{M}_n(t) = \bar{\chi} \mathbf{H}_n(t) = \eta_n \mathbf{M}_0(t)$ within the linear response theory, where $\bar{\chi}$ is the magnetic susceptibility tensor and $\mathbf{M}_0(t) = \bar{\chi} \mathbf{H}_0(t)$.

In the MCh metamolecule, $\mathbf{H}_n(t)$ is governed by the following equation of motion based on Maxwell's equations (33),

$$\left(\frac{d^2}{dt^2} + 2\beta_n \omega_n \frac{d}{dt} + \omega_n^2 \right) \mathbf{h}_n = -\eta_n \left(\frac{d^2}{dt^2} + 2\beta_n \omega_n \frac{d}{dt} \right) m_x \hat{\mathbf{x}}, \quad (\text{S5})$$

with an effective damping of the chiral cavity photon modes expressed as $\beta_n = \sigma/(2\varepsilon\omega_n)$. σ , ε , and m_x represent the electrical conductivity of the copper, the permittivity of YIG, and the x -component of magnetization, \mathbf{M}_0 , of YIG normalized by the saturation magnetization, M_s , respectively. Furthermore, $\mathbf{h}_n(t) = \mathbf{H}_n(t)/M_s$ is introduced as a normalized vector for the AC magnetic fields of the chiral cavity photon. The right-hand side of Eq. (S5) reflects the effect of Faraday's electromagnetic induction. In contrast, the magnetization dynamics for a uniform magnon mode are described by the Landau-Lifshitz-Gilbert equation:

$$\frac{d\mathbf{m}}{dt} = -\gamma\mathbf{m} \times \left(-\frac{1}{M_s} \frac{\delta U_m}{\delta \mathbf{m}} + \mu_0 M_s \sum_n \mathbf{h}_n(t) \right) + \alpha\mathbf{m} \times \frac{d\mathbf{m}}{dt}. \quad (\text{S6})$$

Here, the total magnetic energy for the YIG cylinder is derived by

$$U_m = -\mu_0 M_s \mathbf{m} \cdot \mathbf{H}_{\text{ext}} + \frac{1}{4} \mu_0 M_s^2 (1 - m_x^2), \quad (\text{S7})$$

where $\mathbf{H}_{\text{ext}} = H_{\text{ext}} \hat{\mathbf{z}}$ is the external static magnetic field. The second term on the right-hand side of Eq. (S7) corresponds to the demagnetization field effect of a cylinder shape.

We numerically solve the coupled Eqs. (S5) and (S6) to evaluate the coupling ratio. Here, we consider that the mode-index of the chiral resonance is $n = 3, 5$ based on a simulation using COMSOL Multiphysics. We investigate the Rabi-like oscillation between the chiral cavity photons ($h_{n,x}$) and the magnon (m_x) under 0.39 T for $n = 3$ and 0.50 T for $n = 5$, respectively. In Figs. 3B and 3C, we set an initial condition of the damped oscillations: $\mu_0 \mathbf{H}_0(t = 0) = 2$ mT. Furthermore, the net magnitude of the AC resonant magnetic field should be inversely proportional to the number of antinodes; therefore, $\eta_n = 1/n$ is assumed. For material parameters, we use $\beta_3 = \beta_5 = 10^{-4}$ and $\alpha = 10^{-3}$ for polycrystalline YIG, $\mu_0 M_s = 200$ mT, and $\gamma = 1.76 \times 10^{11} \text{ T}^{-1} \text{ s}^{-1}$.

Supplementary Text

Transmission spectra measured and simulated without DC magnetic fields

Figure S2A illustrates the simulated $|S_{21}|$ spectra of the magnetic YIG meta-atom (black), Cu chiral meta-atom (blue), and MCh metamolecule (red) oriented in the x -direction. The simulated spectrum of the magnetic YIG meta-atom with 1 mm displaced in the x -direction is also presented as $|S_{21}| \times 20$ by another black curve. The simulated $|S_{21}|$ spectra of the z -direction oriented meta-atoms and a metamolecule are illustrated in Fig. S2B. Figure S2C illustrates the experimentally measured $|S_{21}|$ spectra of the magnetic YIG meta-atom (black), Cu chiral meta-atom (blue), and MCh metamolecule (red) oriented in the x -direction. Figure S2D illustrates the experimentally measured $|S_{21}|$ spectra of the magnetic YIG meta-atom (black), Cu chiral meta-atom (blue), and MCh metamolecule (red) oriented in the z -direction.

Figure S2A reveals that the YIG meta-atom at the waveguide center exhibits no dip for the numerically simulated spectra of the x -axis oriented samples. Contrastingly, the chiral meta-atom exhibits a dip at approximately 13.5 GHz, which is assigned to the third-order resonance with two nodes in the chiral structure from the surface current distribution. By inserting the YIG meta-atom into the chiral meta-atom and constructing an MCh metamolecule, the third-order chiral resonance shifts to a lower frequency at approximately 10.5 GHz, as shown by the surface current distribution in Movie S1. Additionally, the simulation of the MCh metamolecule indicates that another dip -- toroidal-like mode shown in Movie S2 -- appears at approximately 13 GHz.

Figure S2C presents the corresponding measured spectra. The metamolecule oriented to the x -axis exhibits two dips at approximately 9.5 GHz (a) and 12.5 GHz (b) in the measured spectrum. The dip (a) is probably traced back to the third-order resonance observed at approximately 10.5 GHz in the simulated spectrum in Fig. S2A. In this study, we focus on this mode labeled (a). In Fig. S2C, (a) is shifted to a higher frequency by removing the YIG meta-atom from the metamolecule and appears at 11.5 GHz according to the numerical results in Fig. S2A. The dip (b) at 12.5 GHz in Fig. S2C is not caused by the toroidal-like mode observed at approximately 13 GHz in the simulated spectrum in Fig. S2A but by the Mie resonance from the YIG meta-atom because the YIG meta-atom in Fig. S2C shows a small dip at 12.5 GHz labeled (#). In contrast, the chiral meta-atom does not present the dip. The additional numerical simulation in Fig. S2A reveals that a YIG cylinder with 1 mm displaced in the x -direction reproduces a dip at approximately 12.5 GHz. The surface current distribution of this mode indicates an electric Mie resonance in the YIG cylinder as a dielectric cavity. Another dip labeled (*) in Fig. S2C is an artifact by the WR-90 waveguide because the dip is observed with an empty waveguide in the measurements.

In Fig. S2B, the numerical simulation of the MCh metamolecule in the z -direction shows three dips at approximately 7.5 GHz, 10.5 GHz, and 13.5 GHz. Surface current distributions indicate that these dips are traced back to the 2nd, 3rd, and 4th order resonances, respectively. In this molecular orientation, odd- and even-number modes can be excited. Comparing Fig. S2A and S2B revealed that the frequency of the identical chiral resonance mode is independent of the metamolecule orientation. Therefore, a dip labeled (f) in the measured spectrum of the z -axis oriented metamolecule in Fig. S2D is traced back to the third-order resonance as the mode (a) in Fig. S2C. The dip (g) is likely to be caused by the fourth-order mode. The dip (h) and (i) are caused by the Mie resonance of the slightly displaced YIG meta-atom (#) and the artifact of the waveguide (*), respectively.

Experimental results of z -axis oriented metamolecule

Figure S3A presents a measurement setup for S parameters of the metamolecule oriented to the z -axis. Figure S3B illustrates $|S_{21}|$ spectra at various $\mu_0 H_{\text{ext}}$. Without the magnetic field, four dips labeled (f), (g), (h), and (i) are observed. The dip labeled (h) is assigned to the Mie resonance by the YIG cylinder. Additionally, the dip labeled (i) is caused by the unknown artifact of the waveguide. Therefore, we focus on dips (f) and (g) in the following. By applying $\mu_0 H_{\text{ext}}$, the dips are shifted to a higher frequency. Additionally, the magnon resonance denoted by (j) appears at 180 mT. Figure S2C presents a 2D plot of $|S_{21}|$, highlighting anti-crossing with the level splitting of chiral cavity photons. The coupling ratio of the chiral cavity photon (f) and magnon (j) is $g/\omega_a = 0.11$, which is smaller than that observed with the x -oriented metamolecule in Fig. 2A. Figure S2D presents the $|S_{21}|$ - $|S_{12}|$ 2D plot at this sample orientation. Non-reciprocal signals are observed at signals (f) and (g).

Non-reciprocal spectra of the x -axis oriented metamolecule

Figures S4A and S4B present the transmission amplitude difference $|S_{21}| - |S_{12}|$ and phase difference ($\arg S_{21} - \arg S_{12}$) spectra of the metamolecule in the x -axis orientation, respectively. In Fig. S4A, the dip (a) becomes the peak (a') after it is passed by the magnon signal (c). This is a clear signature of directional non-reciprocity by the MCh effects. Similarly, in Fig. S4B, the dispersion shape of signal (a) is inverted as (a') after it is passed by the magnon signal (c).

Summary of magnon polariton in this study

Table S1 compares the magnon-polariton obtained in this study with those reported in several studies (Nb, niobium; Py, permalloy; aluminum oxide, AlO_x; yttrium iron garnet, YIG; YBa₂Cu₃O₇, YBCO; platinum, Pt; copper, Cu). This study reports the cavity-free, ultrastrongly-coupled, and non-reciprocal magnon-polariton at room temperature.

Modes of the chiral cavity photon

Movie S1 reveals that the mode at 10.6 GHz is traced back to the third-order resonance with two nodes. Contrastingly, Movie S2 establishes that the mode at 12.9 GHz is not caused by the simple fifth-order mode but by a toroidal-like mode with toroidal current distribution on the Cu chiral structure.

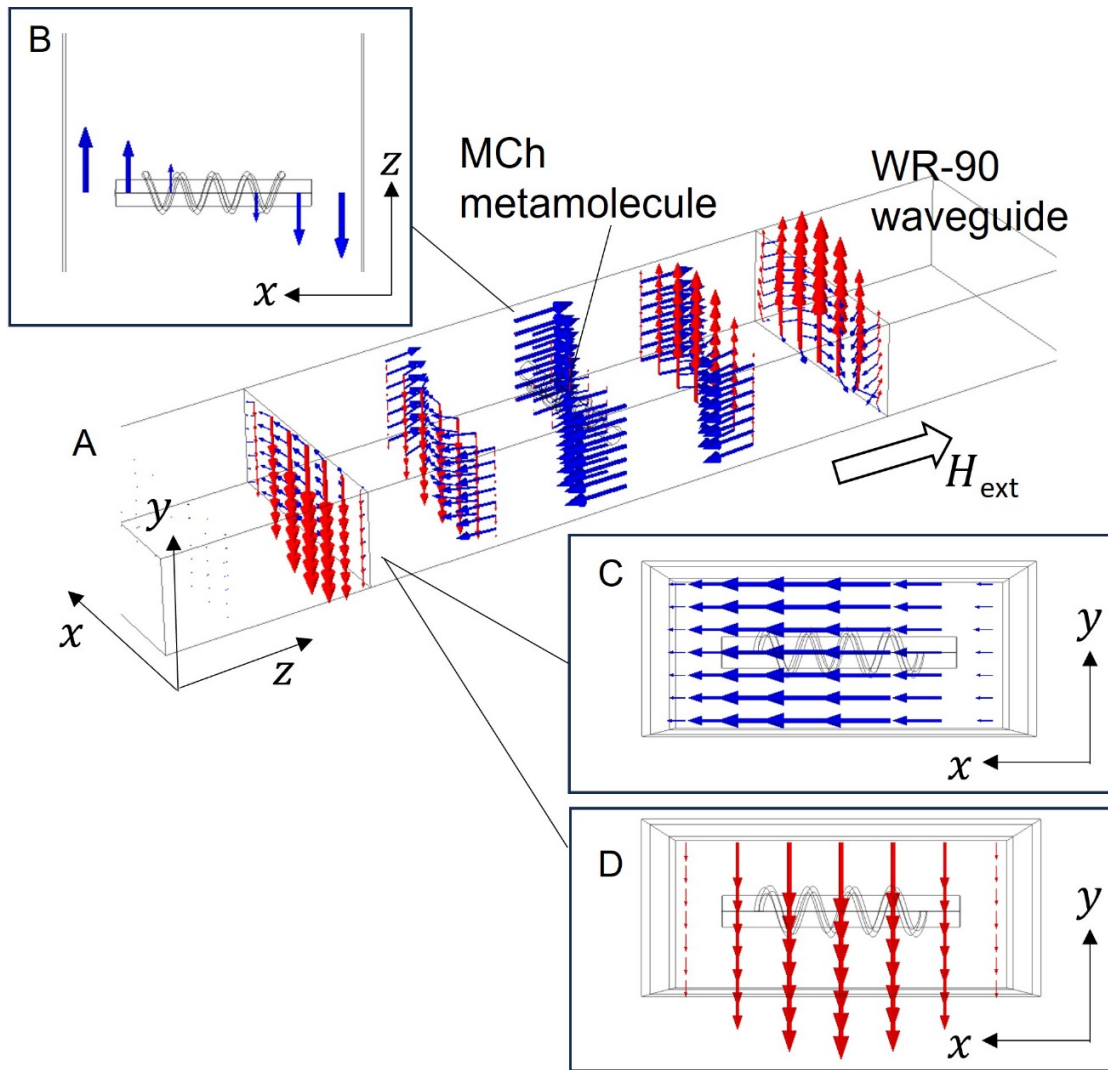


Fig. S1.

(A) A snapshot of the numerically simulated AC magnetic field (blue) and electric fields (red) of the TE_{10} mode traveling wave in the WR-90 waveguide. (B) The magnetic fields in the x - z plane. (C) The magnetic fields and (D) electric fields in the x - y plane.

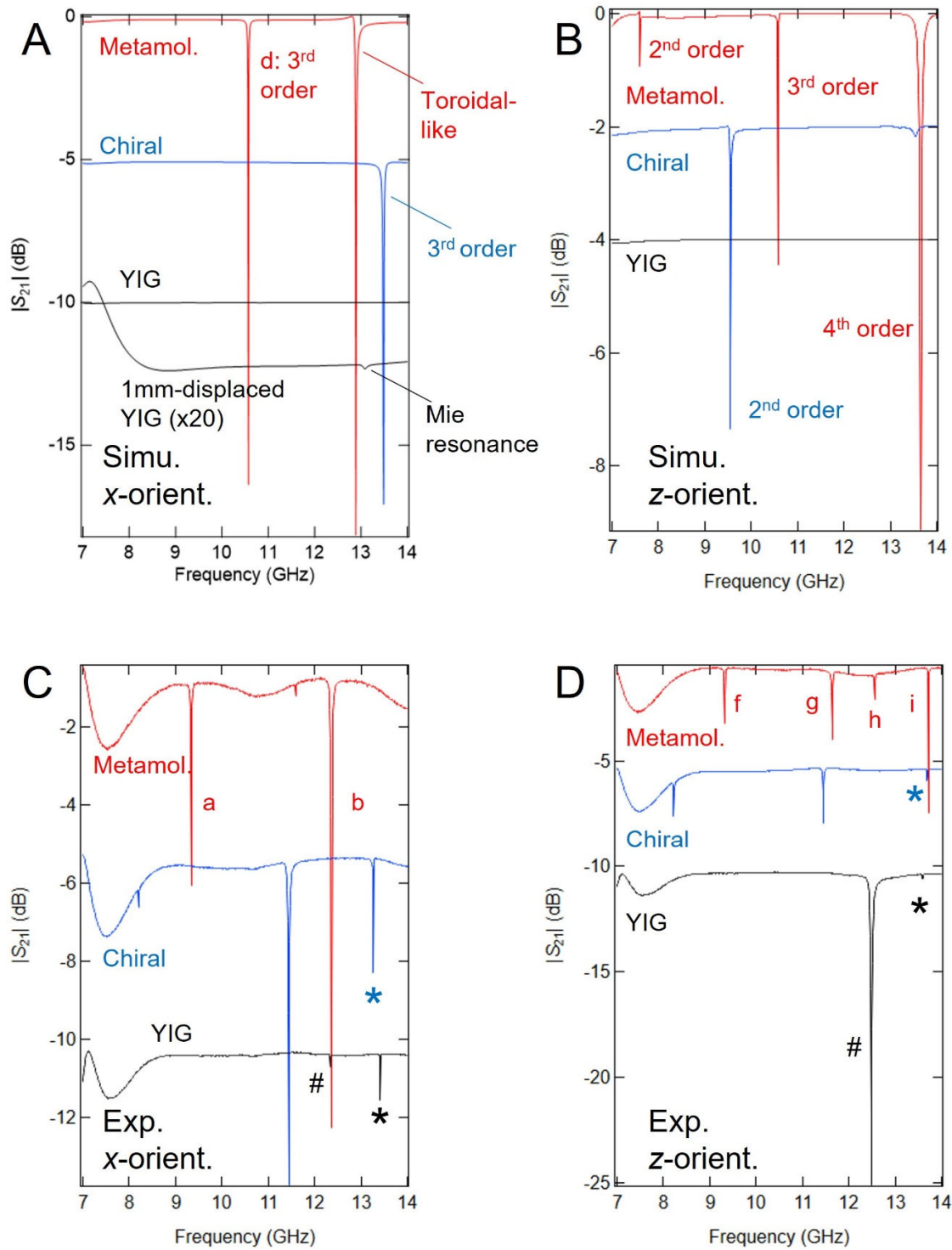


Fig. S2.

Simulation results using COMSOL of the (A) x - and (B) z -axis oriented metamolecule (red), chiral meta-atom (blue), and YIG meta-atom (black). Measurement results of the (C) x - and (D) z -axis oriented metamolecule, chiral meta-atom, and YIG meta atom.

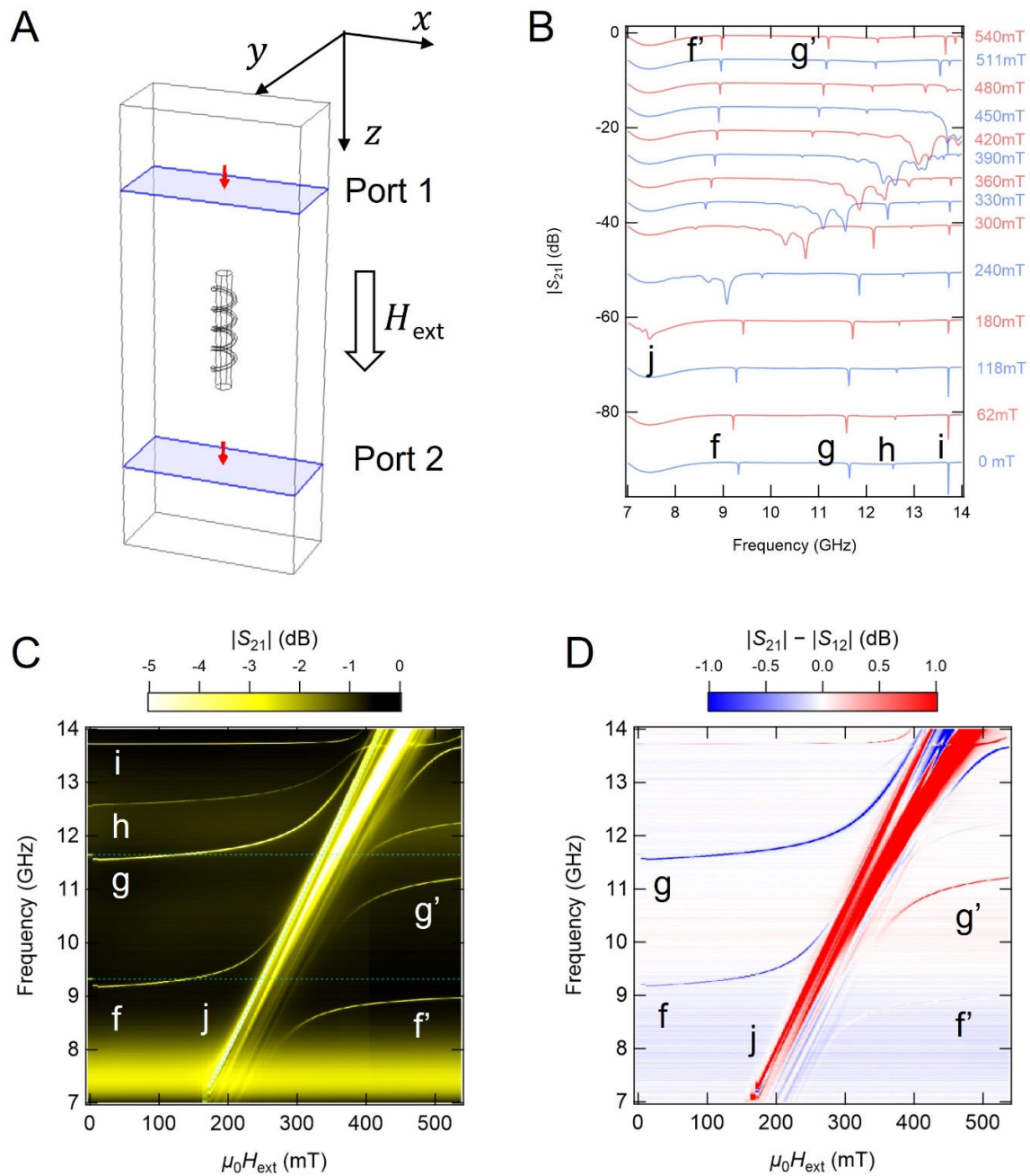


Fig. S3.

(A) Measurement setup of the z-axis oriented metamolecule, (B) $|S_{21}|$ amplitude spectra under various magnetic fields, (C) measured 2D plot of $|S_{21}|$, and (D) measured 2D plot of $\arg(S_{21}) - \arg(S_{12})$ as functions of applied external DC magnetic field and frequency of z-axis oriented metamolecule.

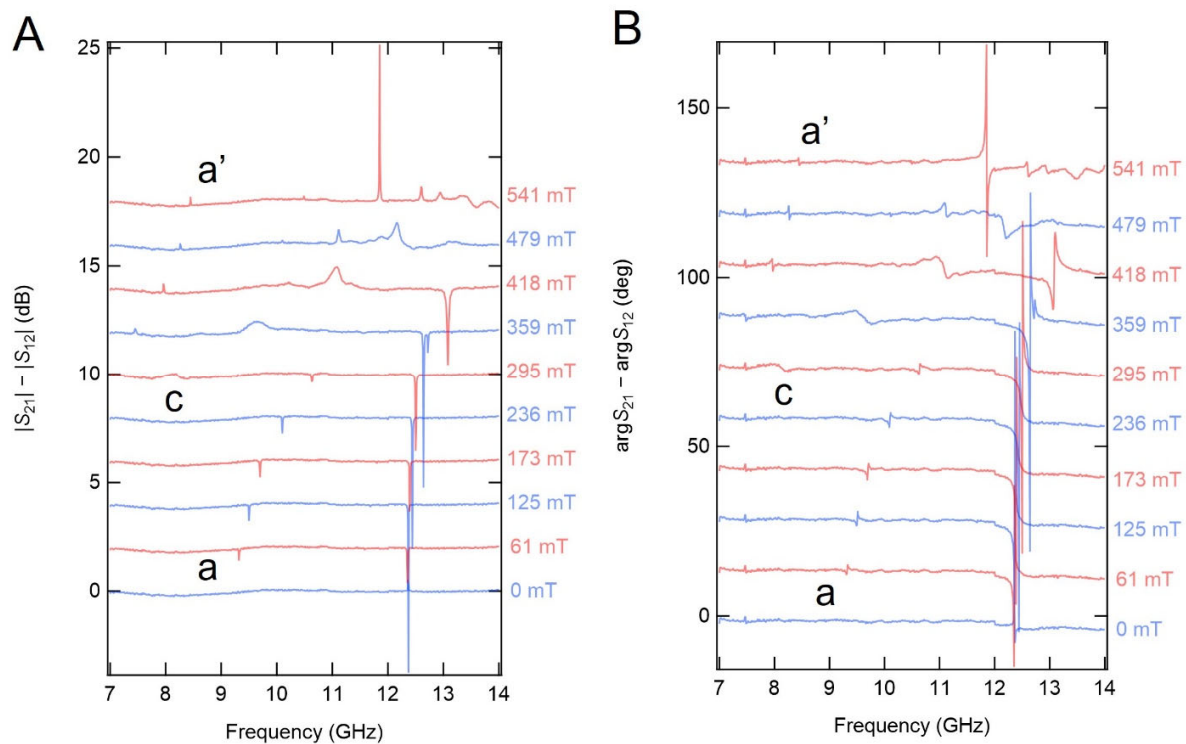


Fig. S4.

Measured (A) amplitude difference, $|S_{21}| - |S_{12}|$, spectra and (B) phase difference, $\arg(S_{21}) - \arg(S_{12})$, spectra of the x-axis oriented metamolecule under various magnetic fields.

Table S1.

Comparison of the sample, temperature, cavity-free, magnon polariton coupling ratio, and non-reciprocity obtained in this study with those reported in several studies (Nb, niobium; Py, permalloy; aluminum oxide, AlO_x; yttrium iron garnet, YIG; YBa₂Cu₃O₇, YBCO; platinum, Pt; copper, Cu).

Sample	Temperature	Cavity-free	g/ω	Non-reciprocity	Ref.
Nb-Py-AlO _x trilayer	< 9K	✓	0.6		[9]
Nb-Py-Nb trilayer	< 9K	✓	0.43		[10]
YIG on YBCO	~ 30K	✓	0.23		[11]
YIG slab	RT		0.59		[6]
MCh metamol.	RT	✓	0.22	✓	This study
YIG sphere	RT		0.01	✓	[14]
YIG sphere	RT		0.067		[34]
YIG-Pt bilayer	RT		0.007		[35]